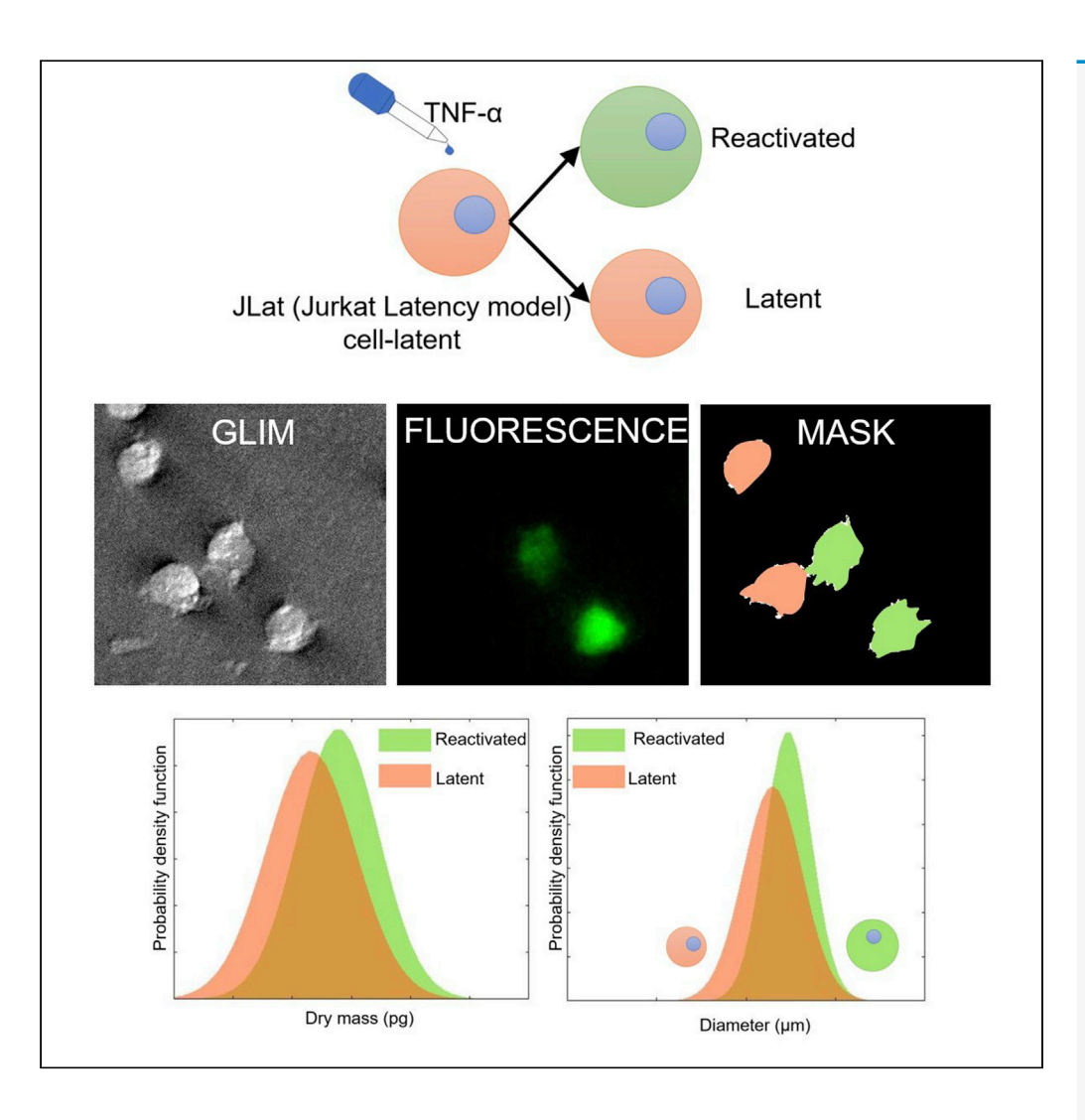
## **iScience**



## **Article**

## Monitoring reactivation of latent HIV by label-free gradient light interference microscopy



Neha Goswami, Yiyang Lu, Mikhail E. Kandel, ..., Erin N. Tevonian, Roy D. Dar, Gabriel Popescu

roydar@illinois.edu (R.D.D.) gpopescu@illinois.edu (G.P.)

#### Highlights

GLIM imaging reveals differences between latent and reactivated HIV in JLat cells

Cells with reactivated HIV have higher dry mass and diameter

Goswami et al., iScience 24, 102940 August 20, 2021 © 2021 https://doi.org/10.1016/ j.isci.2021.102940



## **iScience**



#### **Article**

# Monitoring reactivation of latent HIV by label-free gradient light interference microscopy

Neha Goswami,<sup>1,3</sup> Yiyang Lu,<sup>1,4</sup> Mikhail E. Kandel,<sup>2,3</sup> Michael J. Fanous,<sup>1,3</sup> Kathrin Bohn-Wippert,<sup>1,4</sup> Erin N. Tevonian,<sup>1,4</sup> Roy D. Dar,<sup>1,2,4,\*</sup> and Gabriel Popescu<sup>1,2,3,5,\*</sup>

#### **SUMMARY**

Human immunodeficiency virus (HIV) can infect cells and take a quiescent and nonexpressive state called latency. In this study, we report insights provided by label-free, gradient light interference microscopy (GLIM) about the changes in dry mass, diameter, and dry mass density associated with infected cells that occur upon reactivation. We discovered that the mean cell dry mass and mean diameter of latently infected cells treated with reactivating drug, TNF- $\alpha$ , are higher for latent cells that reactivate than those of the cells that did not reactivate. Cells with mean dry mass and diameter less than approximately 10 pg and 8  $\mu$ m, respectively, remain exclusively in the latent state. Also, cells with mean dry mass greater than approximately 28-30 pg and mean diameter greater than 11–12  $\mu$ m have a higher probability of reactivating. This study is significant as it presents a new label-free approach to quantify latent reactivation of a virus in single cells.

#### INTRODUCTION

Human immunodeficiency virus (HIV) is a global pandemic with over 38M infected individuals. Host cells infected by HIV may either actively produce new viral particles or stay in a dormant state called latency, where they are capable of evading detection and drug treatments and start viral production upon perturbations. Despite the effectiveness of antiretroviral therapies (ARTs) to treat the actively replicating virus to below the limit of detection, the establishment and existence of the latent cell reservoir remains the major barrier to an HIV cure (Dahabieh et al., 2015; Richman et al., 2009; Ruelas and Greene, 2013; Siliciano and Greene, 2011). Upon removal of ARTs, the latent HIV reservoir of cells reactivates and reinitiates active replication of the virus to original viral levels in the blood. Viruses have been studied for underlying mechanisms establishing latency, and microscopy has been used to characterize gene regulation and viral decision-making at the single-cell level (Bohn-Wippert et al., 2018; Hansen et al., 2018; Weinberger et al., 2005, 2008; Zeng et al., 2010). As a fluorescence-based model system for studying HIV latency may not always be available, label-free imaging methods may become more popular and are in higher demand. Label-free imaging of HIV-infected cells allows the observation of viral behavior without the need for a reporter-based system.

Biological samples are mostly transparent to visible light, resulting in low-contrast bright-field images. The immediate solution in the early days was to resort to fluorescent staining for enhanced contrast. However, fluorescence staining is known to perturb the function of live cells (Hoebe et al., 2007). Furthermore, fluorescence imaging produces sample photobleaching and phototoxicity (Boudreau et al., 2016; Hoebe et al., 2007), thus preventing long-term observations. The key to overcome the contrast limitation and to avoid the drawbacks of fluorescence is to use a phase-sensitive imaging modality. Phase information stems from the fluctuations in the optical path length introduced by the sample itself. The first such method was Zernike's phase-contrast microscopy (Zernike, 1955) in which a phase of  $\pi/2$  is introduced between incident and scattered field components. Phase-contrast microscopes enhance the contrast of biological samples significantly. Another advance in mitigating low contrast was the introduction of differential interference contrast (DIC) (Lang, 1982) microscopy, wherein the contrast is provided by the interference of laterally sheared and orthogonally polarized fields traversing the sample. These methods fall into the

<sup>1</sup>Department of Bioengineering, University of Illinois at Urbana-Champaign, Urbana, IL 61801, USA

<sup>2</sup>Department of Electrical and Computer Engineering, University of Illinois at Urbana-Champaign, Urbana, IL 61801, USA

<sup>3</sup>Quantitative Light Imaging Laboratory, Beckman Institute for Advanced Science and Technology, University of Illinois at Urbana-Champaign, Urbana, IL 61801, USA

<sup>4</sup>Everitt Laboratory, University of Illinois at Urbana-Champaign, Urbana, IL 61801, USA

<sup>5</sup>Lead contact

\*Correspondence: roydar@illinois.edu (R.D.D.), gpopescu@illinois.edu (G.P.) https://doi.org/10.1016/j.isci. 2021.102940







category of qualitative phase imaging methods, where contrast is increased, but phase information cannot be extracted quantitatively.

In order to extract quantitative information from unlabeled specimens and take advantage of progress in light sources, modulation devices, and photodetectors, recently quantitative phase imaging (QPI) has developed very rapidly. QPI (Popescu, 2011) is the field of microscopy methods that measure phase information from the specimens of interest. This capability enabled a broad range of biomedical applications (refer to the study by Park et al., 2018 for a review). QPI has been applied to investigations of cell growth (Kandel et al., 2019c; Lee et al., 2017; Mir et al., 2011; Sridharan Weaver et al., 2019), neuron dynamics (Cintora et al., 2017; Fan et al., 2017; Hu and Popescu, 2018; Hu et al., 2019a; Wang et al., 2011a), intracellular mass transport (Wang et al., 2011b), red blood cell properties (Popescu et al., 2005, 2006, 2007), fertility outcomes in cattle (Rubessa et al., 2019, 2020), etc. Since it provides intrinsic markers such as dry mass and optical path length change, it has been successful in revealing new and crucial information in histopathology (Majeed et al., 2019; Takabayashi et al., 2018, 2019), prostate cancer (Nguyen et al., 2017c), breast cancer (Majeed et al., 2018), colorectal cancer (Kandel et al., 2017), pancreatic cancer (Fanous et al., 2020), skin cancer (Li et al., 2019), blood screenings (Mir et al., 2010), pelvic organ prolapse (Hu et al., 2019b), and kidney injury (Ban et al., 2018). Recent advances in deep learning allow the development of phase imaging with computational specificity, where synthetic fluorescence is generated computationally from label-free data (Kandel et al., 2020).

GLIM is a recently developed QPI system that combines phase shifting, common path, and white light configurations, which makes it extremely stable and sensitive (Kandel et al., 2019b; Nguyen et al., 2017). In this study, we implemented GLIM for high-throughput well plate scanning to study the reactivation of latent HIV in a latency model established in Jurkat cells (JLat 9.2) (Dar et al., 2014; Jordan et al., 2003). We used the intrinsic cellular dry mass from the GLIM data to study the reactivation of the latent virus. We found that reactivated cells exhibit statistically larger dry mass than latent ones, while the dry mass density remains comparable between the two populations.

#### **RESULTS**

#### **GLIM** imaging

Reactivation of latent HIV in JLat 9.2 cells (Jordan et al., 2003) was previously studied using flow cytometry (Bohn-Wippert et al., 2017; Dar et al., 2014; Lu et al., 2021) and fluorescence microscopy (Bohn-Wippert et al., 2018), both using fluorescent probes expressed along with the viral genome. In a previous study (Bohn-Wippert et al., 2018), it was reported that reactivation occurred in cells with larger diameter. As a control experiment, T cell activation and cell size were shown to be independent of one another using anti-CD69 antibody staining and flow cytometry. An aim of the current study was to determine the applicability of quantitative phase imaging, specifically GLIM (Figure 1), to understand the science behind cellular dynamics upon HIV reactivation from latency. The use of GLIM allows extraction of properties that fluorescence cannot provide. Since this is the first study of HIV reactivation through GLIM, the fluorescence channel from a reporter vector of HIV was simultaneously monitored to draw the parallel.

JLat 9.2 cells were plated according to standard Cell-Tak protocol (see STAR Methods section). Tumor necrosis factor alpha (TNF-α), a drug that reactivates HIV from latency (Folks et al., 1989), was added at a concentration of 10 ng/mL to the plated cells right before the time-lapse imaging. Figure 1A shows the GLIM imaging setup. Dual-channel imaging, comprising of simultaneous GLIM and fluorescence acquisition, time-lapse imaging, was performed on the sample for 24 hr. Workflow is shown in Figures 1B and 1C. Upon reactivation, cells emit green fluorescence signal due to expression of a green fluorescent protein (GFP). In all repeats of the experiment, reactivation occurred at about 8–10 hr after the drug addition. The percent reactivation of the whole-cell population is about 20% around 20 hr after TNF-α addition. These are consistent with previous reports (Bohn-Wippert et al., 2018). JLat 9.2 cells are inherently in a latent state. These cells never reactivate or produce GFP signal without drug perturbations, which was utilized as the control group in all the experiments to test this claim. No fluorescence signal was observed in the control group. GLIM can provide quantitative phase information of the cells under study. Dual-channel imaging provided phase maps along with fluorescence maps for each frame. Acquired phase information is intrinsic and does not require the use of any genetic modification or staining of the sample. This enables cellular imaging in their unperturbed form. The genetic





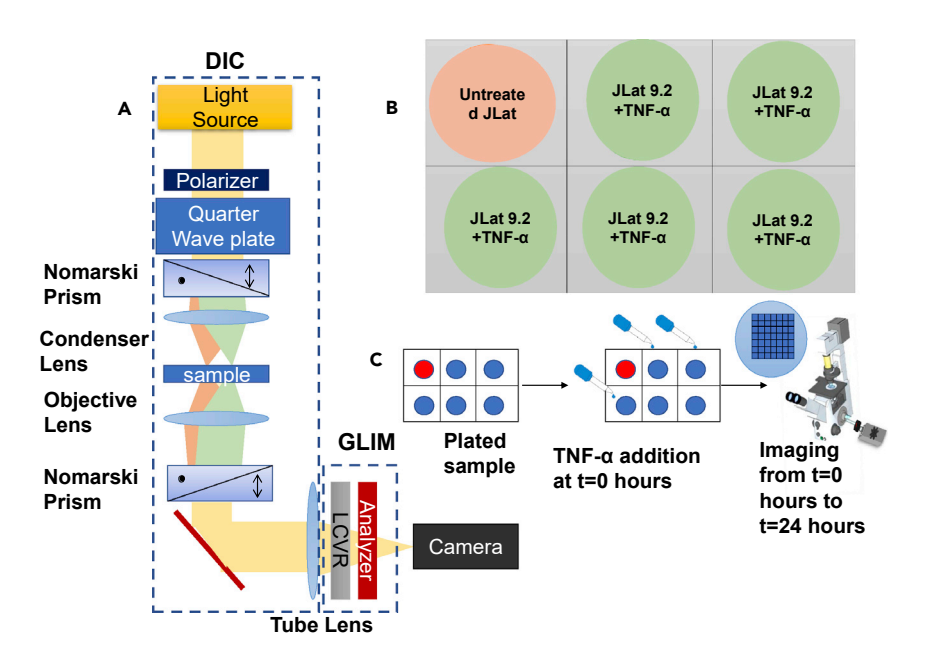


Figure 1. Experimental details

(A) GLIM imaging setup: GLIM module is attached to a standard DIC microscope where a liquid crystal variable retarder (LCVR) adds three additional phases in increments of  $\pi/2$  to one of the two orthogonally sheared polarization beams. (B) Cells were plated in a 6-well plate with untreated JLat 9.2 cells as control and replicates of JLat 9.2 treated with 10 ng/mL TNF- $\alpha$ .

(C) Experiment flow: TNF- $\alpha$  was added at t = 0 hr followed by imaging on a dual-channel (GLIM + fluorescence) microscope; inset shows the 7 x 7 scanning grid per well.

structure of the JLat 9.2 is shown in Figure 2A. Figure 2B shows the results obtained through GLIM imaging. Time-lapse imaging was performed for 24 hr showing the progression of reactivation in Figure 2C where the first frame shows the reactivation that started at nearly 9 hr after TNF- $\alpha$  addition (Bohn-Wippert et al., 2018).

#### Reactivated cells exhibit a higher dry mass and larger cell diameter

Images from both channels, GLIM and fluorescence, were registered and segmented to extract dry mass, diameter, and dry mass density of individual cells. Single-cell tracking (meaning, positions of individual cells were tracked over time) was performed to quantify reactivation at the cellular level. Results of these processing steps are shown in Figure 3 (see STAR Methods section and Figures S1 and S2). Note that the tracking result has memory of all the time frames, which is why there are tracks where the cells once were, detached, and left the frame. Two types of processing techniques were used. One was the bulk processing (see STAR Methods section and Figures S3 and S4), where the quantity of interest was averaged over all cells in the entire frame and in time. It provided a coarse and quick analysis. We also used a second, more detailed analysis, in which quantities were averaged over time for each single cell. We also repeated the experiment for other JLat clones, namely JLat 10.6 and JLat 15.4, to assess the generality of our results to additional integration sites. Figure 4 shows the results of the single-cell tracking method for JLat 9.2, 10.6, and 15.4 cells. Temporal averages of cell dry mass (M) (Figures 4A, 4E, and 4G)) (see STAR Methods section, (Equation 6)) and diameter (D) (Figures 4B, 4F, and 4H)) show higher dry mass and diameter for cells with reactivated HIV. On the other hand, change in dry mass density  $(\rho)$  for JLat 9.2 (Figure 4C) (see STAR Methods section, (Equation 5)) is small compared with the other two measures. These histograms also provide us the range of each measure. There were cells with diameter as low as 6 µm to as high as 18 µm. Similarly, the observed dry mass ranges from 8 pg to 60 pg. Thus, it can be concluded that the temporal mean (signifying individual cell trend, Figure 4) displays a significant difference in mean diameter and dry mass between the cells that reactivated and those that did not, with 1-way ANOVA test yielding p values<0.001 (exact values shown in Figures 5A-5C). These observations are not integration site dependent, as the same trend is observed in all three JLat clones, with slight but negligible differences in the overall range of values of diameter and dry mass. These results are





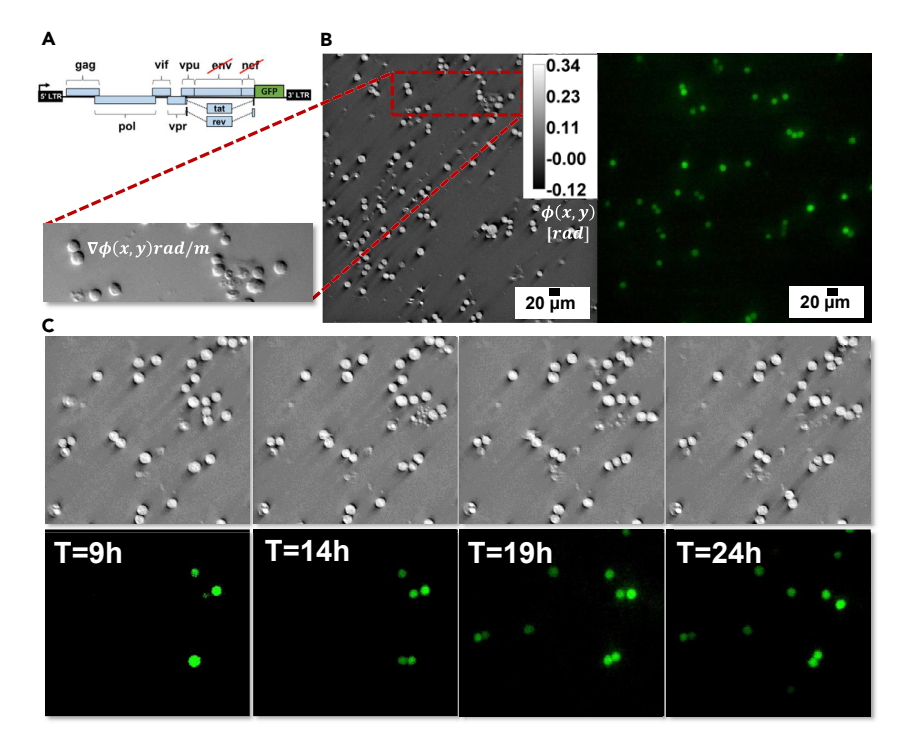


Figure 2. Correlative GLIM and fluorescence imaging

(A) JLat 9.2 is a clonal cell line derived from Jurkat T cells, infected with a full-length HIV gene circuit, with a deletion of the env reading frame and a replacement of nef reading frame by GFP (Jordan et al., 2003).

(B) Quantitative phase image obtained from GLIM after integrating the phase gradient map (shown in inset) and fluorescence map for the same field of view. Imaging was done using DIC 20x/0.8 objective and FITC filter for fluorescence, scale bar:  $20~\mu m$ 

(C) 24-hr time-lapse imaging results. Reactivation of HIV from latency was first observed around 8–10 hr after drug addition. Frames in 5-hr intervals are shown.

compatible with the detected difference in diameter observed between latent and reactivated cells in a previous study (Bohn-Wippert et al., 2018).

#### Cell dry mass provides a measure of reactivation, while dry mass density does not

Difference in dry mass density was not as evident as the differences observed in diameter and dry mass. This implies that dry mass density remains a biological constant between latent and reactivated states of HIV in JLat 9.2 cells. This is further proved by receiver operating characteristic (ROC) curves in Figure 4D, where the areas under the curve (AUCs) for dry mass and diameter are nearly the same (0.64 and 0.63, respectively), while the AUC for dry mass density is 0.55, which shows its limitation in characterizing differences between the two states. Another piece of evidence is the statistical result shown in Figures 5A–5C, where the p value of mean dry mass density is significant yet highest among the three measures. Similar statistical results from the Kruskal-Wallis test are shown in Figure S5 with p values<0.0001. The dependency of dry mass and dry mass density on area is illustrated in Figures 5D–5G. Dry mass density has negligible correlation with area for both 'On' and 'Off' cells (Figures 5D and 5E). Dependence of dry mass on area is higher for both, reactivated ('On') cells (Figure 5G) and latent ('Off') cells (Figure 5F). This higher dependency of dry mass on area is expected following the relationship in Equation 6 (see STAR Methods section).

#### **Exclusive and probable latency regime**

Apart from the differences in mean dry mass and diameter, additional information was extracted from the histograms in Figure 4. It can be seen that individual cells with temporal mean dry mass less than approximately 10 pg and temporal mean diameter less than approximately 8  $\mu$ m stay exclusively in the latent state. However, note that the total number of cells in these exclusive regimes is very small as compared with the total population. On the other hand, it can also be inferred that cells with mean dry mass and diameter smaller than 28-30



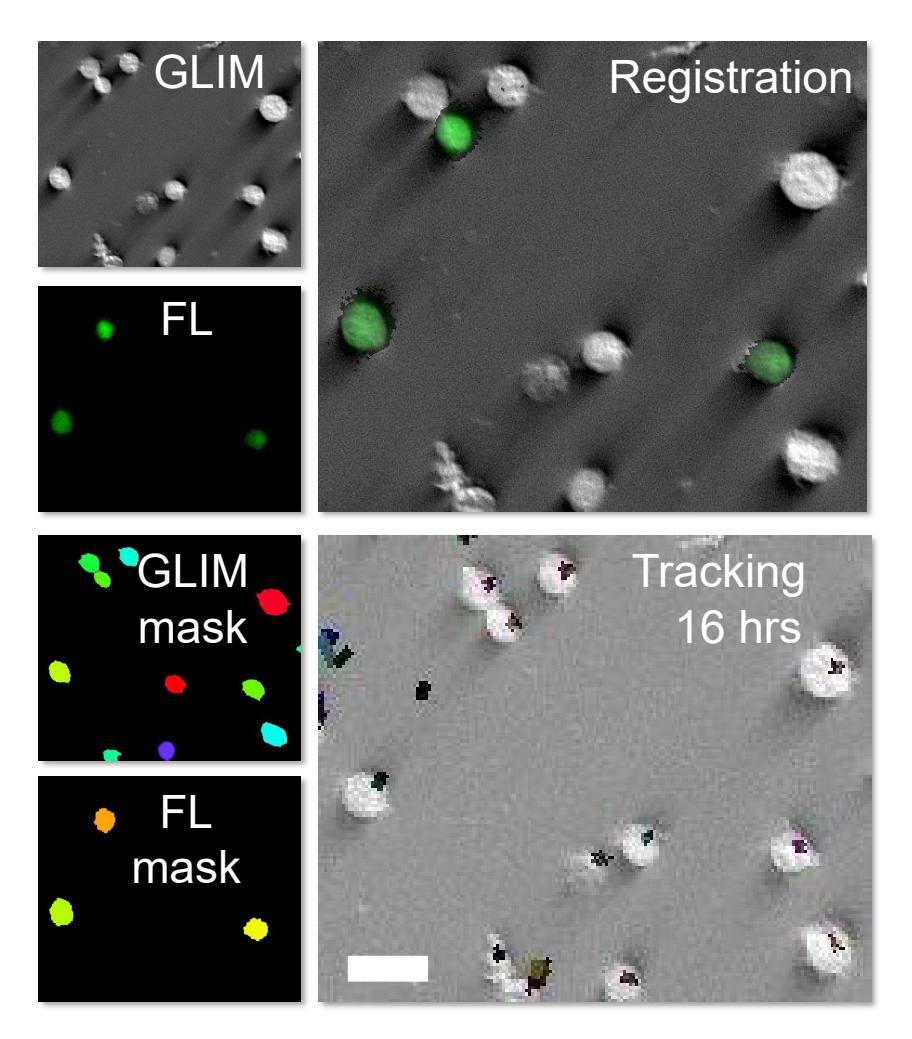


Figure 3. Processing workflow

GLIM and fluorescence (FL) masks were prepared from GLIM and fluorescence images (GLIM and FL), respectively. GLIM and FL were registered to overlay them perfectly. Single-cell tracking was performed for 16 hr (from the ninth hour after reactivation to 24 hr). Single-cell trajectories are shown in the tracking window. Scale bar:  $20 \, \mu m$ 

pg and  $11-12 \,\mu m$ , respectively, have a higher probability of staying latent, while the ones with mean dry mass, diameter greater than these corresponding values, have a higher probability of being reactivated.

#### Time trends of reactivated HIV

The reactivation of HIV in JLat 9.2 cells due to the action of TNF- $\alpha$  was a slow process, with the first reactivation event observed around 8–10 hr after drug addition, as shown in Figure 2C. The average ratio of reactivated and latent cells per frame is plotted with respect to time in Figure 6A. Data follow a linear trend. The range of % 'On' observed is consistent with reactivation previously observed for JLat 9.2 (Bohn-Wippert et al., 2017; Dar et al., 2014). Fluorescence intensity averaged over cells per time bin is shown in Figure 6B where the red curve corresponds to the mean background pixel values of latent or nonfluorescent cells. Figure 6C shows the mean dry mass trend for reactivated cells and latent cells over time. The rate of decay of dry mass of 'Off' cells is higher than that of 'On' cells.

#### Mode of reactivation

Analysis of time-lapse images reveals some key modes of the reactivation process. Different modes of reactivation were observed at the cellular level (Video S1). The first and most prominent mode is growth. Cells grow in size and reactivate. Another method is cell division. Reactivated cells upon division retain the reactivation state in each of the daughter cells.



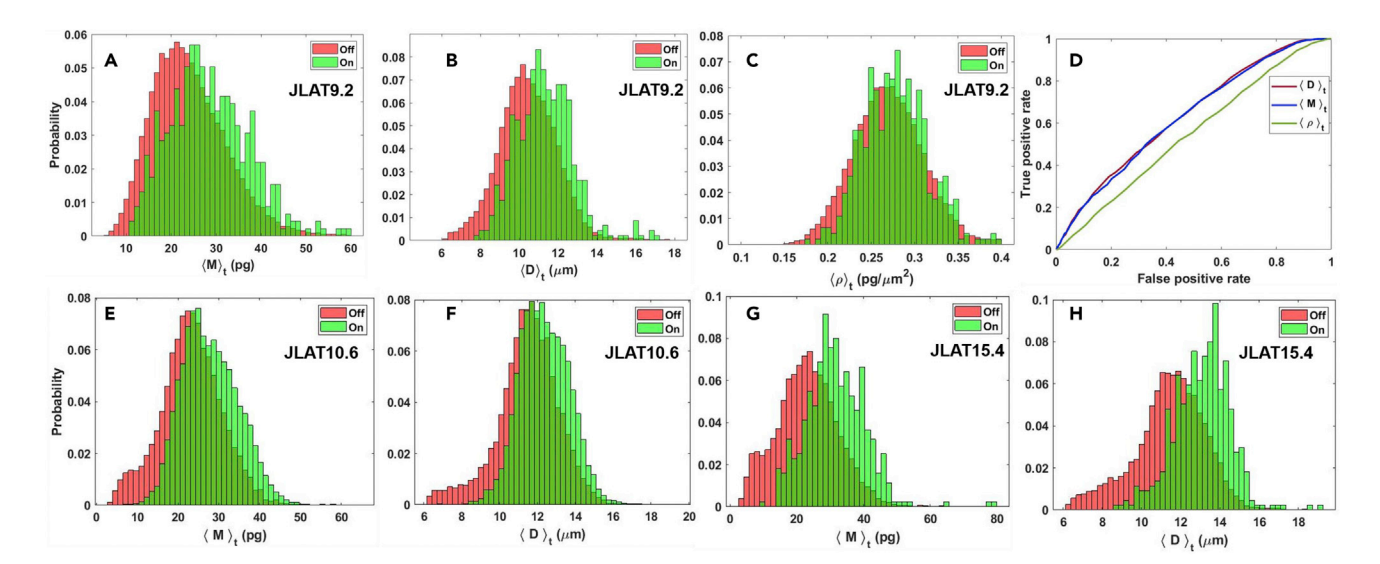


Figure 4. Single-cell processing result

(A-C) Histogram of temporal average of (A) dry mass (M), (B) diameter (D), and (C) dry mass density  $(\rho)$  for JLat 9.2 cells. Legend denotes reactivated cells by "On" and latent cells by "Off."

(D–H) (D) ROC curves for the three quantities. The area under curve is 0.63, 0.64, and 0.55 for dry mass (M), diameter (D), and dry mass density (ρ), respectively. Results on repeats of experiment on two different JLat clones with temporal average of (E) dry mass (M) and (F) diameter (D) for JLat 10.6 and temporal average of (G) dry mass (M) and (H) diameter (D) for JLat 15.4. All three JLat clones show the same trend of reactivated cells having higher dry mass and diameter than latent cells.

#### **Control experiments**

To determine the validity of our results, several control experiments were carried out. We tested our results against three variables: effect of exclusion of detached cells on size distribution, effect of exclusion of detached cells on % reactivation, and effect of TNF- $\alpha$  addition on size distribution. Since all the measurements in this study are based on the cells that remain adhered to the 6-well plate, the detached cells were not analyzed. However, to determine the effects of exclusion of detached cells, additional flow cytometry experiments involving suspension cells were carried out, as explained in STAR Methods section. The % reactivation events captured for both adherent and suspension cells match the trend with highest reactivations occurring in JLat 10.6 cells and lowest in JLat 15.4 cells, proving that % reactivation trend is not affected by the exclusion of detached cells (Figure S6). The diameter distribution is similar for both cases, with mean diameter of adhered cells measured to be about 11.5  $\mu$ m and 12.8  $\mu$ m for suspension cells (Figure S7). Both these results imply that we can safely neglect detached cells without biasing the findings of this study. To determine the effects of TNF- $\alpha$  on the cell size distribution, we measured the size of cells before and after TNF- $\alpha$  addition using an automated cell counter (MOXI Z, Orflo) (see STAR Methods section). We found that the addition of TNF- $\alpha$  does not affect the cell size distribution (Figure S8).

#### **DISCUSSION**

We demonstrated the utility of label-free, intrinsic measures derived from GLIM in understanding the differences between latent and reactivated states of HIV. Our results obtained with GLIM agree with the cell diameter trend shown in a previous study using fluorescence imaging (Bohn-Wippert et al., 2018). In addition to the diameter, GLIM provides new intrinsic measures such as dry mass and dry mass density. These measures also reflect the change between latency and reactivation upon addition of an activator treatment. The results show that cells with higher dry mass and diameter have a higher probability of being in the reactivated state than the latent state. However, dry mass is a stronger measure than the dry mass density. This result suggests that while reactivation is correlated with heavier cells, this is achieved by an increase in the overall size, while the density appears to be a biological constant.

The HIV long terminal repeat (LTR) promoter exhibits a switching behavior between an actively transcribing "on" state and a nontranscriptive "off" state, with a much faster rate of switching to the "off" state than to the "on" state (Singh et al., 2010). This produces bursty gene expression behavior where the gene exhibits short

## iScience Article



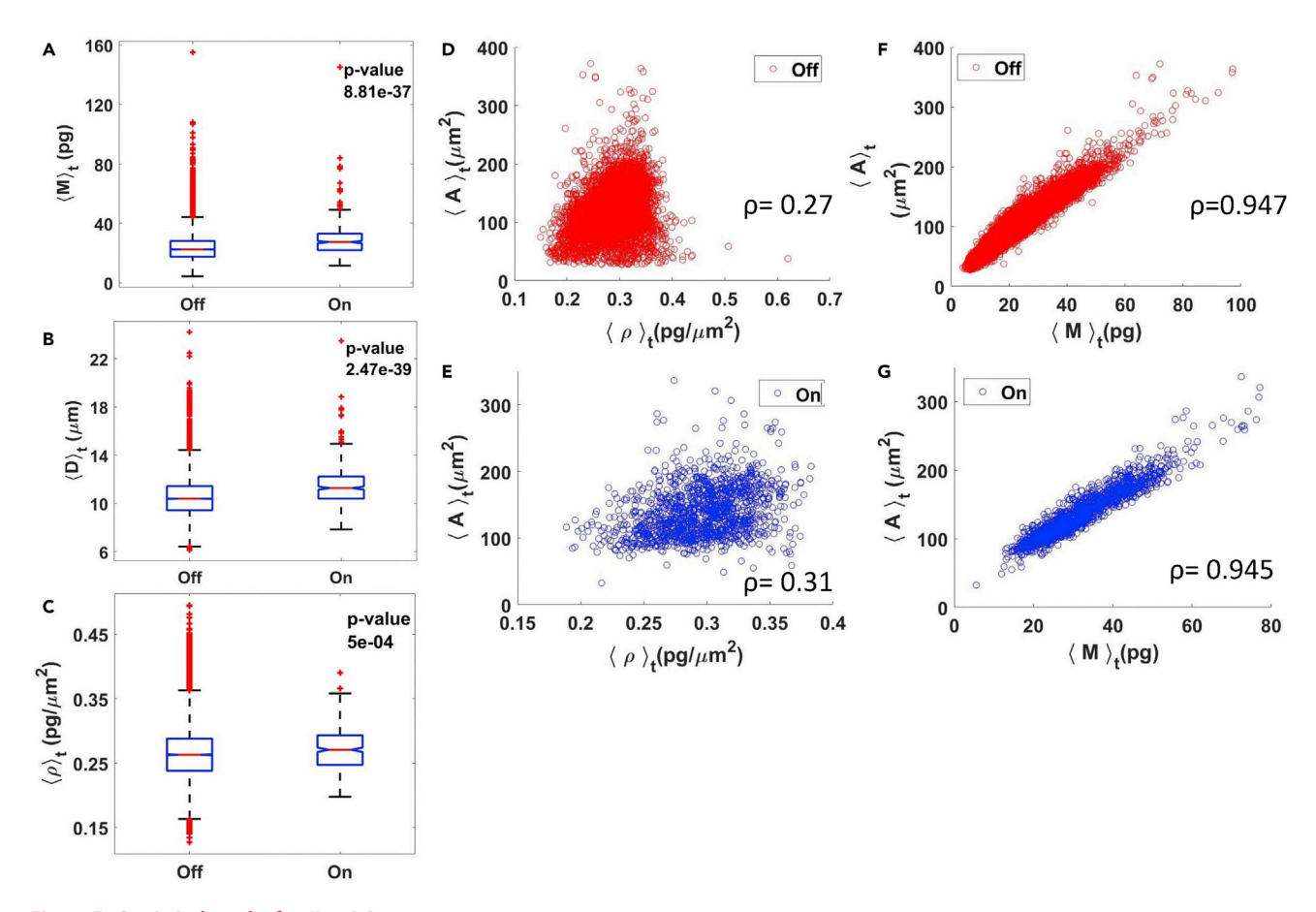


Figure 5. Statistical results for JLat 9.2

(A–G) One-way ANOVA for temporal average of (A) dry mass (M),  $p = 8.81 \times 10^{-37}$ , (B) diameter (D),  $p = 2.47 \times 10^{-39}$ , and (C) dry mass density ( $\rho$ ),  $p = 5 \times 10^{-4}$ . Each quantity exhibits p < 0.001 denoting significance. Sample size is 24,418 for the "Off" group and 445 for the "On" group. Dry mass and diameter are suitable choices for measures of reactivation because of lower p value, indicating higher difference, than dry mass density. Scatterplot of area and dry mass density for (D) "Off" and (E) "On" cells, showing no dependency. However, there is an observable dependency between area and dry mass for both (F) "Off" and (G) "On" cells. Pearson's correlation coefficients are shown on each plot.

bursts of transcription activity with long durations of no transcription. TNF primarily increases HIV's burst frequency (the rate of switching from "off" to "on"), and previous research has shown that transcriptional burst size (or the number of mRNA produced per activity pulse) increases with cell size (Padovan-Merhar et al., 2015). Increases of burst frequency and burst size together increase mean protein abundance, suggesting that the combination of TNF treatment and large cell size can potentially achieve the high protein abundances needed for viral reactivation. This may explain why "on" cells in this study are larger than their "off" cell counterparts. This phenomenon has also been observed in primary CD4+ HIV latency models where cells exclusively reactivate at larger cell sizes (Bohn-Wippert et al., 2018) and with synergistic drug cocktails tailored to enhance HIV reactivation by simultaneously increasing both burst size and burst frequency (Dar et al., 2014).

While the changes in size alone can be monitored using flow cytometry, GLIM has many advantages over flow cytometry. GLIM is a label-free quantitative microscopy technique, which enables measurement of "phase information" of the sample without external tags or stains. Quantities such as dry mass that indicate nonaqueous cell mass are then derived from the phase information. No extensive sample preparation is required as all the information is inherent in the sample itself. Also, GLIM is a wide-field measurement, enabling thousands of cells to be imaged and quantified at one imaging time point. Flow cytometry, on the other hand, uses a cell-by-cell measurement process. In contrast to fluorescence microscopy or flow cytometry, the label-free nature of GLIM allows time-lapse observations of the sample over many days, without any risk of photobleaching or phototoxicity.





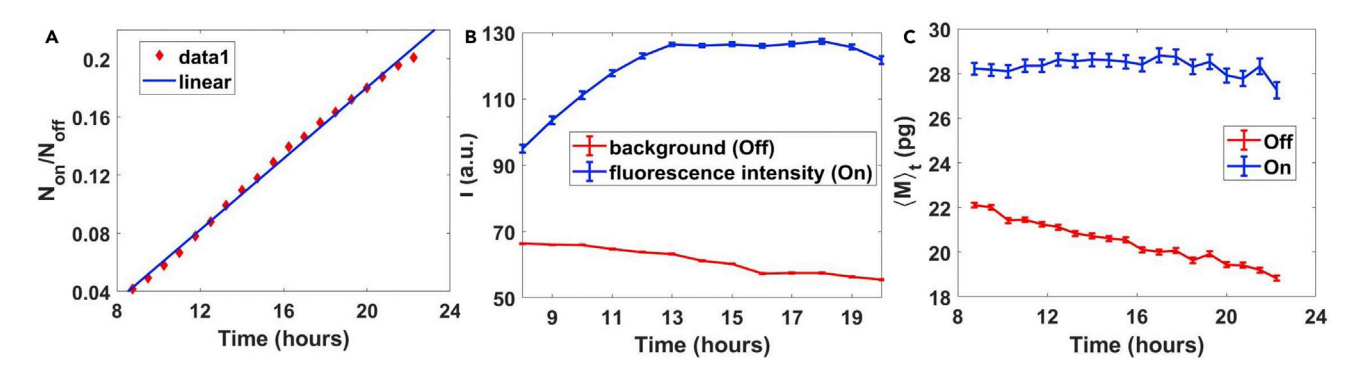


Figure 6. Time trend analysis of reactivated cells for JLat 9.2

(A) Fraction of reactivated cells follow a growth curve, fitted with linear fit.
(B and C) (B) Mean intensity trend for reactivated, fluorescent cells (blue) and mean background pixel values for latent, nonfluorescent cells (red) (C) Mean dry mass time trend for reactivated (On) and latent (Off) cells. Error bars on (B) and (C) indicate standard mean error.

GLIM provides the ability to observe HIV reactivation events in terms of intrinsic cellular markers such as dry mass. For the extraction of these intrinsic markers, GLIM does not require any fluorescent tagging. In this study, we monitored the changes in dry mass and diameter, measured through GLIM, in reactivated cells detected using the fluorescence signal. The focus of this study sought to quantify the differences measured through GLIM in dry mass and dry mass density for reactivated and latent cells identified using fluorescence. Classification of latent and reactivated cells through GLIM may be a future application.

GLIM has the potential to help researchers investigate various biological phenomena, based on intrinsic cell properties. This is as close as possible to track the natural cellular behavior *in vitro*, as the chemical or genetic composition of the cell is not altered. The cells above and below dry mass cutoffs can be predicted to be latent or reactivated with a high likelihood, and any measurement optimization that accentuates the cutoffs will improve such a prediction. This study provides deeper insights into the changes incurred by cells upon HIV reactivation in terms of both size and mass. The findings of this study are significant as they prove the potential of QPI in the field of virology. Our study lays the first foundation of utilizing the power of QPI in the study of HIV and potentially other viruses. HIV reactivation from latency has been shown to be cell cycle dependent (Bohn-Wippert et al., 2018), and this phenomenon will be studied through GLIM in the future. Ultimately these studies will help with the label-free evaluation of the efficiency of therapeutic strategies aiming to remove the latent cell reservoir and cure HIV (Archin et al., 2012; Deeks, 2012).

#### Limitations of the study

Investigation of intrinsic measures of reactivated and latent cells using GLIM required the use of a fluorescent reporter to distinguish between the two cell types. In our future studies, we will explore the potential of GLIM to detect the reactivated cells directly from the label-free data. Recent studies have shown that advances in deep learning algorithms paired with label-free imaging can provide an opportunity to replace fluorescence with specificity algorithms (Kandel et al., 2020). Although currently we are able to find differences between intrinsic measures of latent and reactivated cells using GLIM, classification of the latent and reactivated cell states through GLIM is subject to future studies.

#### **STAR**\*METHODS

Detailed methods are provided in the online version of this paper and include the following:

- KEY RESOURCES TABLE
- RESOURCE AVAILABILITY
  - Lead contact
  - Materials availability
  - O Data and code availability
- EXPERIMENTAL MODEL AND SUBJECT DETAILS
  - O Cell line
- METHOD DETAILS
  - O Sample preparation

## **iScience**

#### **Article**



- O Gradient light interference microscopy
- O Dry mass
- GLIM imaging
- Image processing
- O Additional control experiments
- QUANTIFICATION AND STATISTICAL ANALYSIS

#### **SUPPLEMENTAL INFORMATION**

Supplemental information can be found online at https://doi.org/10.1016/j.isci.2021.102940.

#### **ACKNOWLEDGMENTS**

The authors would like to acknowledge the following grants to support this study: National Institutes of Health (R01GM129709, R01CA238191) and National Science Foundation (0939511, 1450962, 1353368) (awarded to G.P.). E.N.T. acknowledges support provided by the Cancer Scholars Program at UIUC. Y.L., K.B-W., and R.D.D. acknowledge support from NIH NIAID (Al120746) and NSF CAREER (1943740). Authors would also like to acknowledge Quantitative Light Imaging Laboratory members, Dr. Chenfei Hu and Yuchen R. He for informative discussions and GLIM instrument support.

#### **AUTHOR CONTRIBUTIONS**

G.P. and R.D.D. proposed the project. Y.L., K.B-W., and E.N.T. designed and performed mammalian cell culture and contributed to protocol development. N.G. and Y.L. prepared the sample. N.G., M.E.K., and M.J.F. performed the dual-channel imaging. Y.L. conducted flow cytometry experiments. N.G. performed image processing and quantitative analysis. N.G. wrote the manuscript with contribution from all authors. G.P. and R.D.D. supervised the project and manuscript preparation.

#### **DECLARATION OF INTERESTS**

G.P. has financial interests in Phi Optics, Inc., which is a company that produces QPI instruments, including the GLIM module used in this study. The rest of the authors declare no competing interests.

Received: January 12, 2021 Revised: May 24, 2021 Accepted: July 30, 2021 Published: August 20, 2021

#### REFERENCES

Archin, N.M., Liberty, A., Kashuba, A.D., Choudhary, S.K., Kuruc, J., Crooks, A., Parker, D., Anderson, E., Kearney, M., and Strain, M. (2012). Administration of vorinostat disrupts HIV-1 latency in patients on antiretroviral therapy. Nature 487, 482–485.

Ban, S., Min, E., Baek, S., Kwon, H.M., Popescu, G., and Jung, W. (2018). Optical properties of acute kidney injury measured by quantitative phase imaging. Biomed. Opt. Express 9, 921–932.

Bohn-Wippert, K., Tevonian, E.N., Lu, Y., Huang, M.-Y., Megaridis, M.R., and Dar, R.D. (2018). Cell size-based decision-making of a viral gene circuit. Cell Rep. *25*, 3844–3857. e3845.

Bohn-Wippert, K., Tevonian, E.N., Megaridis, M.R., and Dar, R.D. (2017). Similarity in viral and host promoters couples viral reactivation with host cell migration. Nat. Commun. 8, 1–11.

Boudreau, C., Wee, T.-L.E., Duh, Y.-R.S., Couto, M.P., Ardakani, K.H., and Brown, C.M. (2016). Excitation light dose engineering to reduce photobleaching and photo-toxicity. Sci. Rep. 6, 30892.

Cintora, P., Arikkath, J., Kandel, M., Popescu, G., and Best-Popescu, C. (2017). Cell density modulates intracellular mass transport in neural networks. Cytometry A *91*, 503–509.

Creath, K. (1988). Phase-measurement interferometry techniques. Prog. Opt. 26, 349–393.

Dahabieh, M.S., Battivelli, E., and Verdin, E. (2015). Understanding HIV latency: the road to an HIV cure. Annu. Rev. Med. *66*, 407–421.

Dar, R.D., Hosmane, N.N., Arkin, M.R., Siliciano, R.F., and Weinberger, L.S. (2014). Screening for noise in gene expression identifies drug synergies. Science 344, 1392–1396.

Deeks, S.G. (2012). Shock and kill. Nature 487, 439–440.

Fan, A., Tofangchi, A., Kandel, M., Popescu, G., and Saif, T. (2017). Coupled circumferential and axial tension driven by actin and myosin influences in vivo axon diameter. Sci. Rep. 7, 1–12.

Fanous, M., Keikhosravi, A., Kajdacsy-Balla, A., Eliceiri, K.W., and Popescu, G. (2020). Quantitative phase imaging of stromal prognostic markers in pancreatic ductal adenocarcinoma. Biomed. Opt. Express 11, 1354–1364.

Folks, T.M., Clouse, K.A., Justement, J., Rabson, A., Duh, E., Kehrl, J.H., and Fauci, A.S. (1989). Tumor necrosis factor alpha induces expression of human immunodeficiency virus in a chronically infected T-cell clone. Proc. Natl. Acad. Sci. 86, 2365–2368.

Hansen, M.M., Wen, W.Y., Ingerman, E., Razooky, B.S., Thompson, C.E., Dar, R.D., Chin, C.W., Simpson, M.L., and Weinberger, L.S. (2018). A post-transcriptional feedback mechanism for noise suppression and fate stabilization. Cell *173*, 1609–1621. e1615.

Hoebe, R., Van Oven, C., Gadella, T.W., Dhonukshe, P., Van Noorden, C., and Manders, E. (2007). Controlled light-exposure microscopy reduces photobleaching and phototoxicity in fluorescence live-cell imaging. Nat. Biotechnol. 25, 249–253.

Hu, C., and Popescu, G. (2018). Quantitative phase imaging (QPI) in neuroscience. IEEE J. Selected Top. Quan. Electronics 25, 1–9.





- Hu, C., Sam, R., Shan, M., Nastasa, V., Wang, M., Kim, T., Gillette, M., Sengupta, P., and Popescu, G. (2019a). Optical excitation and detection of neuronal activity. J. Biophotonics 12, e201800269.
- Hu, C., Santi, M., Adelaja, O., Kajdacsy-Balla, A., Popescu, G., and Kobak, W. (2019b). Imaging collagen properties in the uterosacral ligaments of women with pelvic organ prolapse using spatial light interference microscopy (SLIM). Front. Phys. 7, 72.
- Jordan, A., Bisgrove, D., and Verdin, E. (2003). HIV reproducibly establishes a latent infection after acute infection of T cells in vitro. EMBO J. 22, 1868–1877.
- Kandel, M.E., He, Y.R., Lee, Y.J., Chen, T.H.-Y., Sullivan, K.M., Aydin, O., Saif, M.T.A., Kong, H., Sobh, N., and Popescu, G. (2020). Phase Imaging with Computational Specificity (PICS) for measuring dry mass changes in sub-cellular compartments. Nat. Commun. 11, 1–10.
- Kandel, M.E., Hu, C., Kouzehgarani, G.N., Min, E., Sullivan, K.M., Kong, H., Li, J.M., Robson, D.N., Gillette, M.U., and Best-Popescu, C. (2019a). Epillumination gradient light interference microscopy for imaging opaque structures. Nat. Commun. 10, 1–9.
- Kandel, M.E., Hu, C., Naseri Kouzehgarani, G., Min, E., Sullivan, K.M., Kong, H., Li, J.M., Robson, D.N., Gillette, M.U., Best-Popescu, C., et al. (2019b). Epi-illumination gradient light interference microscopy for imaging opaque structures. Nat. Commun. 10, 4691.
- Kandel, M.E., Lu, W., Liang, J., Aydin, O., Saif, T.A., and Popescu, G. (2019c). Cell-to-cell influence on growth in large populations. Biomed. Opt. Express 10, 4664–4675.
- Kandel, M.E., Sridharan, S., Liang, J., Luo, Z., Han, K., Macias, V., Shah, A., Patel, R., Tangella, K., and Kajdacsy-Balla, A. (2017). Label-free tissue scanner for colorectal cancer screening.
  J. Biomed. Opt. 22, 066016.
- Lang, W. (1982). Nomarski Differential Interference-Contrast Microscopy (Carl Zeiss).
- Lee, Y.J., Cintora, P., Arikkath, J., Akinsola, O., Kandel, M., Popescu, G., and Best-Popescu, C. (2017). Quantitative assessment of neural outgrowth using spatial light interference microscopy. J. Biomed. Opt. 22, 066015.
- Li, Y., Fanous, M.J., Kilian, K.A., and Popescu, G. (2019). Quantitative phase imaging reveals matrix stiffness-dependent growth and migration of cancer cells. Sci. Rep. 9, 1–8.
- Lu, Y., Bohn-Wippert, K., Pazerunas, P.J., Moy, J.M., Singh, H., and Dar, R.D. (2021). Screening for gene expression fluctuations reveals latency-promoting agents of HIV. Proc. Natl. Acad. Sci. 118, e2012191118.
- Majeed, H., Keikhosravi, A., Kandel, M.E., Nguyen, T.H., Liu, Y., Kajdacsy-Balla, A., Tangella,

- K., Eliceiri, K.W., and Popescu, G. (2019). Quantitative histopathology of stained tissues using color spatial light interference microscopy (cSLIM). Sci. Rep. 9, 14679.
- Majeed, H., Nguyen, T.H., Kandel, M.E., Kajdacsy-Balla, A., and Popescu, G. (2018). Label-free quantitative evaluation of breast tissue using Spatial Light Interference Microscopy (SLIM). Sci. Rep. 8, 1–9.
- Mir, M., Ding, H., Wang, Z., Tangella, K., and Popescu, G. (2010). Blood screening using diffraction phase cytometry. J. Biomed. Opt. 15, 027016.
- Mir, M., Wang, Z., Shen, Z., Bednarz, M., Bashir, R., Golding, I., Prasanth, S.G., and Popescu, G. (2011). Optical measurement of cycle-dependent cell growth. Proc. Natl. Acad. Sci. 108, 13124–13129.
- Nguyen, T.H., Kandel, M.E., Rubessa, M., Wheeler, M.B., and Popescu, G. (2017). Gradient light interference microscopy for 3D imaging of unlabeled specimens. Nat. Commun. 8, 210.
- Nguyen, T.H., Sridharan, S., Macias, V., Kajdacsy-Balla, A., Melamed, J., Do, M.N., and Popescu, G. (2017c). Automatic Gleason grading of prostate cancer using quantitative phase imaging and machine learning. J. Biomed. Opt. 22, 036015.
- Padovan-Merhar, O., Nair, G.P., Biaesch, A.G., Mayer, A., Scarfone, S., Foley, S.W., Wu, A.R., Churchman, L.S., Singh, A., and Raj, A. (2015). Single mammalian cells compensate for differences in cellular volume and DNA copy number through independent global transcriptional mechanisms. Mol. Cell *58*, 339–352.
- Park, Y., Depeursinge, C., and Popescu, G. (2018). Quantitative phase imaging in biomedicine. Nat. Photon. 12, 578–589.
- Popescu, G. (2011). Quantitative Phase Imaging of Cells and Tissues (McGraw Hill Professional).
- Popescu, G., Badizadegan, K., Dasari, R.R., and Feld, M.S. (2006). Observation of dynamic subdomains in red blood cells. J. Biomed. Opt. 11, 040503.
- Popescu, G., Ikeda, T., Best, C., Badizadegan, K., Dasari, R.R., and Feld, M.S. (2005). Erythrocyte structure and dynamics quantified by Hilbert phase microscopy. J. Biomed. Opt. 10, 060503.
- Popescu, G., Park, Y., Dasari, R.R., Badizadegan, K., and Feld, M.S. (2007). Coherence properties of red blood cell membrane motions. Phys. Rev. E 76, 031902.
- Richman, D.D., Margolis, D.M., Delaney, M., Greene, W.C., Hazuda, D., and Pomerantz, R.J. (2009). The challenge of finding a cure for HIV infection. Science *323*, 1304–1307.
- Rubessa, M., Kandel, M.E., Schreiber, S., Meyers, S., Beck, D.H., Popescu, G., and Wheeler, M.B. (2020). Morphometric analysis of sperm used for IVP by three different separation methods with

- spatial light interference microscopy. Syst. Biol. Reprod. Med. 66, 26–36.
- Rubessa, M., Lotti, S.N., Kandel, M.E., Popescu, G., and Wheeler, M.B. (2019). SLIM microscopy allows for visualization of DNA-containing liposomes designed for sperm-mediated gene transfer in cattle. Mol. Biol. Rep. 46, 695–703.
- Ruelas, D.S., and Greene, W.C. (2013). An integrated overview of HIV-1 latency. Cell 155, 519–529.
- Siliciano, R.F., and Greene, W.C. (2011). HIV latency. Cold Spring Harb. Perspect. Med. 1, a007096.
- Singh, A., Razooky, B., Cox, C.D., Simpson, M.L., and Weinberger, L.S. (2010). Transcriptional bursting from the HIV-1 promoter is a significant source of stochastic noise in HIV-1 gene expression. Biophys. J. 98, L32–L34.
- Sridharan Weaver, S., Li, Y., Foucard, L., Majeed, H., Bhaduri, B., Levine, A.J., Kilian, K.A., and Popescu, G. (2019). Simultaneous cell traction and growth measurements using light. J. Biophotonics 12, e201800182.
- Takabayashi, M., Majeed, H., Kajdacsy-Balla, A., and Popescu, G. (2018). Disorder strength measured by quantitative phase imaging as intrinsic cancer marker in fixed tissue biopsies. PLoS One 13, e0194320.
- Takabayashi, M., Majeed, H., Kajdacsy-Balla, A., and Popescu, G. (2019). Tissue spatial correlation as cancer marker. J. Biomed. Opt. 24, 016502.
- Wang, R., Wang, Z., Leigh, J., Sobh, N., Millet, L., Gillette, M.U., Levine, A.J., and Popescu, G. (2011a). One-dimensional deterministic transport in neurons measured by dispersion-relation phase spectroscopy. J. Phys. Condens. Matter 23, 374107
- Wang, R., Wang, Z., Millet, L., Gillette, M.U., Levine, A., and Popescu, G. (2011b). Dispersionrelation phase spectroscopy of intracellular transport. Opt. Express 19, 20571–20579.
- Weinberger, L.S., Burnett, J.C., Toettcher, J.E., Arkin, A.P., and Schaffer, D.V. (2005). Stochastic gene expression in a lentiviral positive-feedback loop: HIV-1 Tat fluctuations drive phenotypic diversity. Cell 122, 169–182.
- Weinberger, L.S., Dar, R.D., and Simpson, M.L. (2008). Transient-mediated fate determination in a transcriptional circuit of HIV. Nat. Genet. 40, 466–470.
- Zeng, L., Skinner, S.O., Zong, C., Sippy, J., Feiss, M., and Golding, I. (2010). Decision making at a subcellular level determines the outcome of bacteriophage infection. Cell *141*, 682–691.
- Zernike, F. (1955). How I discovered phase contrast. Science 121, 345–349.





#### **STAR**\*METHODS

#### **KEY RESOURCES TABLE**

REAGENT or RESOURCE	SOURCE	IDENTIFIER
Biological samples		
JLat Cells	NIH AIDS Reagent Program	NIH-ARP Cat#9848-69; RRID: CVCL_8285;
		NIH-ARP Cat#9849-437; RRID: CVCL_8281;
		NIH-ARP Cat#9850-417; RRID: CVCL_8282
Naïve Jurkat Cells	NIH AIDS Reagent Program	NIH-ARP Cat#177-450; RRID: CVCL_0367
Chemicals, peptides, and recombinant prote	ins	
Cell-Tak	Corning Life Science	354241
TNF-alpha	R&D Systems	210-TA
Experimental models: Cell lines		
JLat 9.2	NIH AIDS Reagent Program	NIH-ARP Cat#9848-69; RRID: CVCL_8285
JLat 10.6	NIH AIDS Reagent Program	NIH-ARP Cat#9849-437; RRID: CVCL_8281
JLat 15.4	NIH AIDS Reagent Program	NIH-ARP Cat#9850-417; RRID: CVCL_8282
Software and algorithms		
MATLAB R2019b	MathWorks	RRID:SCR_001622
CellVista Pro	Phi Optics	https://phioptics.com/products/
Other		
Gradient light interference microscopy	Phi Optics	https://phioptics.com/products/
(GLIM) module	(Kandel et al., 2019a; Nguyen et al., 2017)	

#### **RESOURCE AVAILABILITY**

#### Lead contact

The lead contact for this study is Gabriel Popescu (gpopescu@illinois.edu).

#### **Materials availability**

This study did not generate any new materials or reagents.

#### Data and code availability

- All data reported in this paper will be made available by the lead contact upon request.
- All code descriptions are provided in the paper's STAR Methods section and can be made available by the lead contact upon request.
- Any additional information required to reanalyze the data reported in this paper is available from the lead contact upon request.

#### **EXPERIMENTAL MODEL AND SUBJECT DETAILS**

#### **Cell line**

A well-established Jurkat T cell latency model of HIV (JLat) was used in the current study (Jordan et al., 2003). In this model, Jurkat T cells are latently infected with a full-length HIV virus that has a deletion of env and GFP replacing the *nef* reading frame (Figure 2A) (Jordan et al., 2003). JLat 9.2, 10.6, and 15.4, three unique clonal latent cell population with a single integration site (Jordan et al., 2003), were chosen for the current study. JLat 9.2, 10.6, and 15.4 cell lines were obtained through the NIH AIDS Reagent Program from E. Verdin.





#### **METHOD DETAILS**

#### Sample preparation

Cells were plated in 6-well glass-bottomed plates, following standard protocol. To attach JLat cells to the bottom of imaging plates, a master mix containing Cell-Tak adhesive by Corning was first prepared. It was prepared with a mixture of sodium bicarbonate (75 g/L), sodium hydroxide (40 g/L), and Cell-Tak (2.03 g/L) at a volume ratio of 291:5:4. For each well, 187  $\mu$ L of master mix was added, incubated at room temperature for more than 20 minutes, and completely dried off. Next, cells were added to the wells at a concentration of 1.5 x  $10^5$  cells per well, suspended in 187  $\mu$ L of Dulbecco's phosphate-buffered saline (DPBS). Plated cells were incubated at 5% CO<sub>2</sub>, 37°C for 30-60 minutes, and unadhered cells were carefully washed off with Roswell Park Memorial Institute (RPMI) media (w/ 10% fetal bovine serum (FBS) and 1% pen-strep, w/o phenol red). TNF- $\alpha$  was diluted in RPMI media to 10 ng/ml, and 3mL of dilution was added to each well.

Figure 1B represents the well plate organization; one well was used as control to show the absence of GFP signal in untreated JLat 9.2 cells, while the rest were plated with TNF- $\alpha$ -treated JLat 9.2 cells.

#### **Gradient light interference microscopy**

Gradient light interference microscopy (GLIM) (Kandel et al., 2019b; Nguyen et al., 2017) is an advance microscopy method that is based on the concepts of DIC microscopy. A low coherence source (red LED with central wavelength of 690 nm) is used for microscopy, where the microscope is in the DIC configuration. The resulting spatially sheared, orthogonal polarization components are fed to a liquid crystal variable retarder (LCVR) on the output port. The LCVR introduces variable phase shifts  $\varphi_n$  in four increments of  $\pi/2$  between the two sheared beams. Field at the detector plane can be described as follows: (Kandel et al., 2019a; Nguyen et al., 2017)

$$U_d(\overrightarrow{r}) = U(\overrightarrow{r}) + U(\overrightarrow{r} + \delta \overrightarrow{r})e^{i\varphi_n}$$
 (Equation 1)

Intensity is then,

$$I_{d}(\overrightarrow{r}) = \langle U_{d}(\overrightarrow{r})U_{d}^{*}(\overrightarrow{r})\rangle_{t}$$
 (Equation 2)

$$I_{d}(\overrightarrow{r}) = \langle U_{d}(\overrightarrow{r})U_{d}^{*}(\overrightarrow{r})\rangle_{t} \qquad \text{(Equation 2)}$$
 
$$I_{d}(\overrightarrow{r}) = I(\overrightarrow{r}) + I(\overrightarrow{r} + \delta \overrightarrow{r}) + 2\sqrt{(I(\overrightarrow{r})I(\overrightarrow{r} + \delta \overrightarrow{r}))}\cos(\varphi(\overrightarrow{r} + \delta \overrightarrow{r}) - \varphi(\overrightarrow{r}) + \varphi_{0} + \varphi_{n}) \qquad \text{(Equation 3)}$$

where  $\delta r$  is the spatial displacement between two beams,  $\varphi_0$  is the background phase due to the Nomarski prisms in DIC, and  $\varphi_0 = n\frac{\pi}{2}$ , for n= 0, 1, 2, and 3 is the phase shift introduced by the LCVR for phase-gradient extraction (Kandel et al., 2019a; Nguyen et al., 2017).

The quantity of interest here is  $\varphi(\overrightarrow{r} + \delta \overrightarrow{r}) - \varphi(\overrightarrow{r})$ , which can be expressed in terms of gradient,

$$\varphi(\overrightarrow{r} + \delta \overrightarrow{r}) - \varphi(\overrightarrow{r}) = \nabla_r \varphi \cdot \delta \overrightarrow{r}$$
 (Equation 4)

This phase gradient is then extracted using phase-shifting interferometry algorithm (Creath, 1988; Popescu, 2011), utilizing the four intensity frames captured by varying  $\varphi_n$ . The phase map (Figure 2B) is obtained by integrating the gradient image.

#### **Dry mass**

Dry mass is a measure of nonaqueous content of the cell. Dry mass density, which is the ratio of dry mass to area, is given by the following: (Li et al., 2019)

$$\rho(\mathbf{x},\mathbf{y}) = \frac{\lambda}{2\pi\eta} \varphi(\mathbf{x},\mathbf{y})$$
 (Equation 5)

where  $\lambda$  is the central wavelength of light used,  $\eta = 0.2mL/g$  is the refractive index increment, and  $\varphi(x,y)$  is the phase shift introduced by the sample at spatial location (x,y).

Total dry mass is calculated by taking the surface integral of  $\rho$  over the area of the cell (Mir et al., 2011).

$$M = \frac{\lambda}{2\pi\eta} \iint_{\Delta} \varphi(x, y) dxdy$$
 (Equation 6)

## iScience Article



#### **GLIM** imaging

Cells were plated, and TNF- $\alpha$  was added to all but the first well at time t=0 hour. Sample was then taken for dual-channel time-lapse imaging on the GLIM microscope. Each well was divided into 7 x 7 grid of frames, with each frame being imaged for both fluorescence and phase gradient per time sampling point. Imaging was done for 24 hours. GLIM microscope is a standard DIC microscope (Zeiss Axio-observer Z1) with GLIM module (Phi Optics) attached to the side port. A cage incubator system is installed on the microscope with temperature and  $CO_2$  set at 37°C and 5%, respectively, for these experiments. Imaging was done using a 20x/0.8 DIC objective. For the fluorescence, FITC filter was used for GFP excitation. Fluorescence lamp power was kept at 50%. Before starting the experiment, GLIM has to be calibrated following a procedure outlined in a previous work (Kandel et al., 2019a) to estimate the phase value associated with the background.

#### **Image processing**

After obtaining the images, they were processed using MATLAB (The MathWorks, Inc). The dual-channel images, phase and fluorescence, needed to be registered to perfectly overlay one on another. They were registered using MATLAB app, 'Registration Estimator'. Followed by registration, images were segmented by custom-built MATLAB codes, to extract binary masks for both phase and fluorescence images. These masks were used to extract underlying region properties from the images, some of which are the cell diameter and total phase of the cell from phase images and mean fluorescence intensity and identity from fluorescence images. Identity here refers to the value "1" assigned to cells of the phase map that are present in the fluorescence map and "0" to the rest. After feature extraction, bulk processing was done by averaging the cellular behavior over one frame. All the cells in one frame at one time instance signify the average behavior of one cell at that time. This is a quicker but coarse processing that provides an estimate of average population behavior.

Bulk processing was done to ascertain the population trend in latent and reactivated states of HIV. Segmentation and data extraction were followed by single-cell tracking. To understand the single-cell behavior over time, single-cell tracking was performed using MATLAB codes developed in-house. Segmented cells were numbered as shown in Figure S2A. Different parameters including cell diameter and centroid were measured for each numbered cell. Each cell in one frame was labeled and tracked over time using Euclidean distance between centroids as a metric. The sensitivity of such detection depends on the initial estimate of velocity of cells. During the course of tracking, this initial estimate of velocity is altered to account for cells that move faster than initial estimated velocity. Figure S2B shows the trajectories for one cell. Figure S2C shows the trajectories for all cells in one frame. It is a cumulative map showing all the trajectories of cells that existed during the time of the experiment. The mean fluorescence intensity for reactivated ("On," green) and background radiation for latent ("Off," red) cells is shown in Figure S2D. The drop in fluorescence intensity is due to photobleaching induced by the high-intensity fluorescence excitation. Tracking was done to calculate temporal mean of the quantities of interest per cell. Single-cell analysis yielded us the range of values that were not provided by the population trend. Spatiotemporal mean is calculated for each frame and is given by

$$\mu_{\rm st} = \frac{1}{N_{\rm t}} \sum_{t}^{\sum_{c} a_c} N_c$$
 (Equation 7)

where  $N_t$  is the number of time frames,  $N_c$  is the number of cells per frame, and  $a_c$  is the quantity per cell.

Temporal mean is defined for each cell tracked over time

$$\mu_t = \frac{1}{N_t} \sum_{r} a_r$$
 (Equation 8)

The entire processing flow is shown in Figures S1 and S2.

To compare both ways of processing, histograms of mean fluorescence intensity are shown in Figure S3 for bulk processing (Figure S3A) and single-cell tracking (Figure S3B). Both convey similar behavior of mean, but bulk processing lacks the range information conveyed by the tails in Figure S3B. However, the well-defined separation of fluorescence intensity between two groups validates our analysis procedure in both cases. The result of bulk processing for dry mass, diameter, and dry mass density is as shown in Figure S4, exhibiting that dry mass (Figure S4A) and diameter (Figure S4B) in case of reactivated cells are larger





than those of latent cells, while no such difference exists for dry mass density (Figure S4C). This finding corroborates with the single-cell analysis results in main text Figure 4.

#### **Additional control experiments**

To compare the % reactivation and size distribution between adhered cells (measured through microscopy) and suspension cells (measured through flow cytometry), we conducted additional experiments. JLat 9.2, 15.4, and 10.6 cells were plated on a 6-well glass-bottomed imaging plate and treated with TNF at 10 ng/mL. At the same time, a separate sample of the three JLat clones were treated with TNF at 10 ng/mL in suspension. Microscopy was carried out immediately after TNF treatment on the adhered cells, and flow cytometry measurements were carried out on the suspension sample 24 hr after the treatment. Results for % reactivation are shown in Figure S6. As can be seen, both adhered and suspension cells follow the same % reactivation trend with the highest reactivation seen in JLat 10.6 and lowest reactivations seen in JLat 15.4.

We also assessed the size distribution of adhered and suspension cells using GLIM and MOXI, respectively. Results shown in Figure S7 indicate that size distributions for adhered and suspension cells are similar.

To compare the effect of TNF- $\alpha$  on the Jurkat cells, MOXI measurement was performed on untreated cells and cells treated with TNF- $\alpha$ . Figure S8 illustrates that there is no significant effect of TNF- $\alpha$  on the size distribution.

#### **QUANTIFICATION AND STATISTICAL ANALYSIS**

Statistical analysis of the resulting data was carried out using MATLAB. Since the sample size is quite large, with n = 445 samples in reactivated ("On") group and n = 24,418 samples in latent ("Off") group for JLaT 9.2 cells, normal distribution was assumed and one-way ANOVA was carried out, with default alpha 0.05. The term samples refer to single cells. Figures 5A–5C show that all three measures have significant difference (p<<0.001), with p values mentioned on the bar plots, between "Off" (latent) and "On" (reactivated) states. To ascertain the validity of results, the Kruskal-Wallis test was also carried out and it gave similar results with p values  $2.43 \times 10^{-32}$ ,  $3.47 \times 10^{-38}$ , and  $5.47 \times 10^{-5}$  for dry mass, diameter, and dry mass density, respectively. The Kruskal-Wallis test was followed by a post hoc test on mean ranks using Scheffe's procedure; results are shown in Figure S5. More details can be found in the Results section of this article.

Calculation of ROC curves was also carried out in MATLAB as described in Results section and Figure 4D. Time trends shown in Figures 6A–6C were plotted using MATLAB. Error bars on Figures 6B and 6C represent standard mean error.